Heavy neutral 2HDM Higgs boson pair production at CLIC energies

Majid Hashemi* and Marieh Molanaei†

Physics Department, College of Sciences, Shiraz University, Shiraz 71946-84795, Iran

(Received 29 June 2023; accepted 20 July 2023; published 8 August 2023)

In this work, the neutral Higgs boson pair production is analyzed at the Compact Linear Collider (CLIC) to be operating at center of mass energies $\sqrt{s} = 1400$ GeV (stage 2) and $\sqrt{s} = 3000$ GeV (stage 3). The Higgs bosons to be searched for are neutral CP even (H) and CP odd (A) within the framework of two Higgs doublet model (2HDM) in the mass range $300 < m_{H/A} < 1000$ GeV. All types of CP-conserving models are studied and the signal observability is evaluated, taking into account the main SM background processes like ZZ, $t\bar{t}$, and the SM-like Higgs boson associated production (hZ). Results are presented for a set of model parameters and Higgs boson masses in terms of signal distributions over the background as well as the integrated luminosity needed for 5σ discovery. It is shown that the heavy mass region is well observable at CLIC in types 3 and 4 in the regions not excluded by LHC so far, while in type 1 the signal observation is challenging due to the large jet multiplicity in the $t\bar{t}$ final state.

DOI: 10.1103/PhysRevD.108.035012

I. INTRODUCTION

Over the past few decades, the Standard Model (SM) of particle physics has been the most reasonable theory of subatomic interactions between elementary particles. The underlying framework, which is based on quantum field theory (QFT), describes the strong, electromagnetic and weak interactions.

One of the biggest achievements of the Large Hadron Collider (LHC) is the observation of a new boson that is considered to be the candidate for the missing element of SM, i.e., the Higgs boson introduced through the Higgs mechanism [1–6]. The announcement by the two collaborations, CMS and ATLAS [7,8], at the LHC experiment led to the Physics Nobel Prize in 2013.

The properties of the observed particle have been verified in various analyses by CMS ([9–12]) and ATLAS ([13–16]). Despite the overall agreement of the measurements with SM predictions, there are still several open problems that motivate theories beyond SM (BSM) including matter-antimatter asymmetry [17], the origin of dark matter that is not contained in the SM [18,19], the sensitivity of the muon anomalous magnetic moment to new physics and its current 3 to 4 standard deviation from SM prediction [20], and the hierarchy problem, i.e., the large difference between the Higgs boson mass (125 GeV) and the Planck mass (10^{19} GeV), etc.

The stability of the observed hierarchy with respect to the quantum corrections to the Higgs boson mass is a motivation for below TeV-scale supersymmetry [21,22]. The theory of supersymmetry provides a natural solution to the hierarchy problem by introducing superparticles that contribute to counterterms in the perturbative series of corrections to the Higgs boson mass. In its minimal form, MSSM needs an extended Higgs sector beyond the SM structure [22]. It turns out that for a supersymmetric theory to work, at least two Higgs doublets are needed to give masses to the particles and their superpartners [23,24]. This is not, of course, the only reason for extended Higgs sectors but is considered as one of the main motivations for the two Higgs doublet model (2HDM) [25,26], which was first introduced as a model for CP violation and natural flavor conservation [27–29]. Because of the more degrees of freedom in the model, 2HDM describes the flavor physics observables [30,31] and electroweak precision measurements [32] better than the SM.

The building blocks of the Higgs sector of the two Higgs doublet model consist of two complex scalar doublets Φ_1 and Φ_2 with their corresponding vacuum expectation values v_1 and v_2 under the requirement of $\sqrt{v_1^2 + v_2^2} = 246$ GeV [33,34]. This is a natural expansion of the SM Higgs sector to two doublets. One of direct consequences of having two complex doublets is the multiplicity of the Higgs bosons: two CP-even scalars h, H, a CP-odd pseudoscalar A and the charged Higgs bosons $H^{\pm}$.

At the alignment limit [35–37], the 2HDM partially aligns with the SM in the sense that one of the Higgs

*majid.hashemi@cern.ch
†mmovlanaei@gmail.com

bosons acquires the same properties as the SM Higgs boson. This alignment is to confirm the observation of the new boson at the LHC which is usually assumed to be the lightest 2HDM scalar (h_{SM}), although there is the so-called twisted scenario where the aligned boson is not the lightest [38].

In a CP-conserving scenario, there are four types of the model characterized by the Higgs boson couplings with up/down-type quarks and leptons that are functions of the ratio of the vacuum expectation values denoted by $\tan\beta$. Therefore $\tan\beta$ plays the key role in 2HDM phenomenology [39].

The SM Higgs boson studies are going on at the LHC including pair production (hh) in different final states by CMS [40–44] and ATLAS [45–48]. However, 2HDM Higgs bosons are searched for in single production mode by CMS [38,49–51] and ATLAS [52–54]. The above scenarios are based on $A \to Zh$, $A \to ZH$, $H \to ZA$, or $H \to hh$ with the mother particle produced in proton-proton collisions. The Higgs conversion modes studied by both CMS and ATLAS are limited to the kinematic requirement $|m_A - m_{h/H}| > m_Z$. Therefore, there are open regions in the 2HDM parameter space especially along the equal masses line $m_A = m_H$ favored by $\Delta\rho$ requirements [55–58].

While LHC analyses continue to search for extra Higgs bosons, other experimental scenarios are also under consideration including LHC luminosity upgrade [59,60] and future lepton colliders, CLIC [61,62], ILC [63], FCC [64], and CEPC [65].

The lepton colliders are of interest due to the following:
(1) providing a cleaner collision event environment and lower QCD background due to the less hadron activity compared to hadron colliders,
(2) better knowledge of the effective center of mass energy and the beam spectrum compared to hadron collisions where parton distribution functions play an important role and
(3) kinematic constraints which make event reconstruction easier. The latter is exploited in the current analysis and will be described in more detail.

In recent works, several search scenarios were introduced within type 1 [66–69], type 3 [70,71], and type 4 [72–74]. These analyses are dedicated to lepton colliders but do not cover the heavy neutral Higgs boson masses beyond 500 GeV. In the current analysis, we explore heavy neutral Higgs bosons with masses up to 1000 GeV at CLIC center of mass energies of 1400 and 3000 GeV known as stages 2 and 3, respectively. Details of the analysis will be presented after a theoretical introduction.

II. THEORETICAL FRAMEWORK

Consider the scalar Higgs sector of the SM Lagrangian as described in the Higgs mechanism:

$$\mathcal{L}_{\Phi}^{\mathrm{SM}} = (D^{\mu}\Phi)^{\dagger}(D_{\mu}\Phi) - \mathcal{V}^{\mathrm{SM}}(\Phi) \tag{1}$$

where D_μ is the covariant derivative and Φ is the complex scalar doublet in the spinor representation of $SU(2)_L$:

$$\Phi = \begin{pmatrix} \phi^{+} \\ \phi^{0} \end{pmatrix}. \tag{2}$$

The renormalizable Higgs potential using one doublet takes the form

$$\mathcal{V}^{\mathrm{SM}} = -\mu^2\Phi^{\dagger}\Phi + \lambda(\Phi^{\dagger}\Phi)^2 \tag{3}$$

with μ and λ as the free parameters of the model describing the mass term and quartic self-interactions among scalars. In this form, λ is required to be positive for the vacuum stability and a nonzero vacuum expectation value is obtained provided that $\mu^2 > 0$.

Extensions of the SM have been extensively studied in the literature, including the real scalar extension [75–81], complex scalar extension [82–86], inert doublet model [87–91], and inert doublet plus a complex scalar [92]. These scenarios try to address the two problems of the nature of dark matter and the origin of the baryon asymmetry. The two Higgs doublet model is also one of the simplest SM extensions with an additional complex scalar doublet:

$$\Phi_i = \begin{pmatrix} \phi_i^{+} \\ (v_i + \rho_i + i\eta_i)/\sqrt{2} \end{pmatrix}, \quad i = 1, 2, \tag{4}$$

and the Lagrangian

$$\mathcal{L}_{\Phi}^{\mathrm{2HDM}} = \sum_{i=1,2}(D_{\mu}\Phi_i)^{\dagger}(D^{\mu}\Phi_i) - \mathcal{V}^{\mathrm{2HDM}} \tag{5}$$

with a symmetric potential including mass terms and Higgs-self interactions as follows:

$$\begin{aligned}
\mathcal{V}^{\mathrm{2HDM}} = {} & m_{11}^2\Phi_1^{\dagger}\Phi_1 + m_{22}^2\Phi_2^{\dagger}\Phi_2 - m_{12}^2(\Phi_1^{\dagger}\Phi_2 + \Phi_2^{\dagger}\Phi_1) \\
& + \frac{1}{2}\lambda_1(\Phi_1^{\dagger}\Phi_1)^2 + \frac{1}{2}\lambda_2(\Phi_2^{\dagger}\Phi_2)^2 \\
& + \lambda_3(\Phi_1^{\dagger}\Phi_1)(\Phi_2^{\dagger}\Phi_2) + \lambda_4(\Phi_1^{\dagger}\Phi_2)(\Phi_2^{\dagger}\Phi_1) \\
& + \frac{1}{2}\lambda_5[(\Phi_1^{\dagger}\Phi_2)^2 + (\Phi_2^{\dagger}\Phi_1)^2].
\end{aligned} \tag{6}$$

The neutral Higgs bosons are obtained through a rotation in the ρ_i and η_i spaces with mixing angles α/β for the CP-even/odd Higgs bosons:

$$h = -\rho_1 \sin\alpha + \rho_2 \cos\alpha$$
$$H = \rho_1 \cos\alpha + \rho_2 \sin\alpha$$
$$A = \eta_1 \sin\beta + \eta_2 \cos\beta$$

while the charged Higgs is related to the charged fields $\phi^\pm$:

$$H^\pm = \phi_1^\pm \sin\beta + \phi_2^\pm \cos\beta. \tag{7}$$

The mixing angle β is also related to the ratio of vacuum expectation values through

$$\tan\beta = \frac{v_2}{v_1}. \tag{8}$$

The Yukawa Lagrangian for the Higgs-fermion interaction with fermions follows the usual form for CP-even Higgs bosons (h, H) while for CP-odd Higgs boson A takes additional $i\gamma^5$ in the vertex:

$$\mathcal{L}_\Phi = \frac{m_f}{v} \sum_{f=u,d,l} \bar{f} f (h + \rho_H^f H - i\rho_A^f \gamma^5 A). \tag{9}$$

This is the form of Higgs-fermion interactions at the alignment limit ($\beta - \alpha = \pi/2$) where the light Higgs coupling with fermions is equivalent with SM predictions. The heavy Higgs boson coupling with fermions, however, deviates from the SM form of m_f/v by the $\rho_{H/A}^f$ values. The ρ_H^f takes the following forms for different types of the model as presented in Table I. The ρ_A^f equals ρ_H^f but takes an extra minus sign for $f = u$. The Higgs-gauge couplings scaled to their corresponding SM values are

$$\frac{g_{hVV}^{\text{2HDM}}}{g_{hVV}^{\text{SM}}} = \sin(\beta - \alpha)$$
$$\frac{g_{HVV}^{\text{2HDM}}}{g_{hVV}^{\text{SM}}} = \cos(\beta - \alpha). \tag{10}$$

The alignment limit requires $\sin(\beta - \alpha) = 1$, thus leading to gaugophobic heavy Higgs bosons while the light 2HDM Higgs boson fully coincides with the SM prediction in terms of the couplings with fermions and gauge bosons.

TABLE I. Higgs-fermion couplings in different types of 2HDM at the alignment limit.

	Model type			
Coupling	1	2	3	4
ρ^u	$\cot\beta$	$\cot\beta$	$\cot\beta$	$\cot\beta$
ρ^d	$\cot\beta$	$-\tan\beta$	$-\tan\beta$	$\cot\beta$
ρ^d	$\cot\beta$	$-\tan\beta$	$\cot\beta$	$-\tan\beta$

III. CROSS SECTION AND DECAY RATES

The signal process under study is $e^-e^+ \to Z^* \to HA$ in the four fermion final state as shown in Fig. 1 with the second vertex set to

$$g_{HAZ} = \frac{-g\sin(\beta - \alpha)}{2\cos\theta_W} \tag{11}$$

which is maximum at the alignment limit. The light Higgs production, i.e., $e^-e^+ \to Z^* \to hA$, involves $g_{hAZ} \propto \cos(\beta - \alpha)$ and vanishes due to suppression of the vertex under the same circumstances.

As for the signal cross section, one can start from the usual differential form of

$$\frac{d\sigma}{d\Omega} = \frac{1}{64\pi^2 s} \frac{p_f}{p_i} \langle |M_{fi}|^2 \rangle \tag{12}$$

where in the center of mass frame, $p_i = \sqrt{s}/2$ and $p_f = \frac{1}{2\sqrt{s}} \sqrt{\lambda(s, m_H^2, m_A^2)}$ with λ being the Källén function defined as $\lambda(\alpha, \beta, \gamma) = \alpha^2 + \beta^2 + \gamma^2 - 2\alpha\beta - 2\alpha\gamma - 2\beta\gamma$. In this case one can write λ as $[s - (m_A + m_H)^2] \times [s - (m_A - m_H)^2]$. The matrix element consists of the Z boson propagator, vertex couplings, and the electroweak coefficients ($g_V^e \simeq -0.04$ and $g_A^e = -0.5$ according to the Particle Data Group [93]) which lead to the following form for the integrated total cross section as a function of the collider center of mass energy $\sqrt{s}$ and the Higgs boson masses m_H and m_A:

$$\sigma = \frac{\pi\alpha^2 (g_V^2 + g_A^2) [[s - (m_A + m_H)^2][s - (m_A - m_H)^2]]^{\frac{3}{2}}}{48 s^2 \sin^4\theta_W \cos^4\theta_W [(s - m_Z^2)^2 + m_Z^2 \Gamma_Z^2]}. \tag{13}$$

According to the above form of Eq. (13), the cross section is suppressed when the sum of the Higgs boson masses

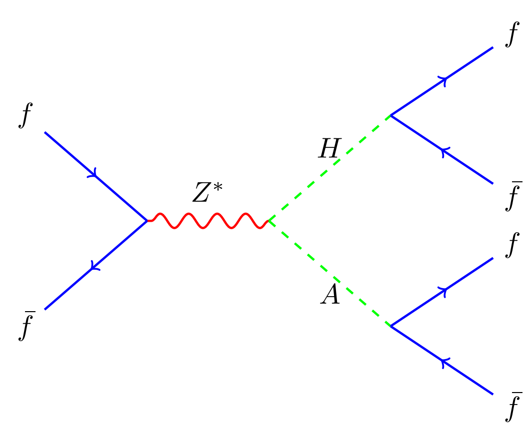

FIG. 1. Feynman diagram of the Higgs boson pair production in the four fermion final state. The fermion f is t-quark in type 1, b-quark in types 2 and 3, and τ-lepton in type 4.

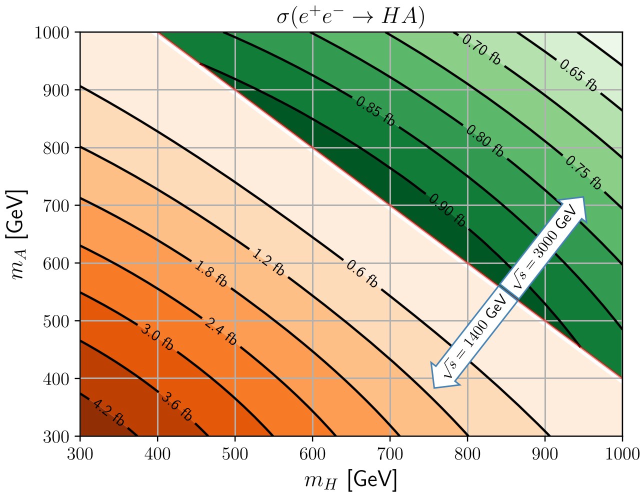

FIG. 2. The signal cross section as a function of the Higgs boson masses for the two center of mass energies of 1400 and 3000 GeV, obtained using WHIZARD with unpolarized beams.

approaches the center of mass energy, receives enhancement at the Z boson pole mass, and prefers equal masses for the Higgs bosons due to the last term in the numerator. As the result a symmetric distribution is expected in the Higgs boson masses space.

The tree level values predicted in Eq. (13) are confirmed by WHIZARD 3.1.2 [94,95]. As an example, with $\sqrt{s} = 1400$ GeV, $m_H = 400$ GeV, and $m_A = 600$ GeV, Eq. (13) yields $\sigma = 2.2$ fb, to be compared with WHIZARD result of $\sigma = 2.1$ fb with unpolarized beams. Including a polarization of 80% (30%) for $e^-(e^+)$ enhances the above value to 3.1 fb. A full scan over the Higgs boson masses in the two regions of $\sqrt{s} = 1400$ and 3000 GeV results in Fig. 2 where different color styles are used to distinguish the two regions of center of mass energies.

The Higgs boson decay to fermion pairs can also be calculated using the square of the matrix element which, keeping the fermion masses, becomes

$$\sum_{\text{spins}} |M_{H/A\to f\bar{f}}|^2 = 4\sqrt{2}G_F m_f^2 (\rho^f)^2 [(p_f.p_{\bar{f}}) \mp m_f^2] \tag{14}$$

where the subtraction (sum) on the right-hand side occurs for CP-even (CP-odd) Higgs bosons, respectively. The four momentum product is related to the particle masses through $s = m_{H/A}^2 = (p_f + p_{\bar{f}})^2 = 2m_f^2 + 2p_f.p_{\bar{f}}$. As a result, CP-even and CP-odd Higgs bosons acquire different decay rates through their matrix elements:

$$\langle |M^2| \rangle = 2\sqrt{2}G_F m_f^2 (\rho^f)^2 \times \begin{cases} m_H^2 - 4m_f^2, & \text{H} \\ m_A^2, & \text{A} \end{cases} \tag{15}$$

which result in ([96,97]):

$$\Gamma(H/A \to f\bar{f}) = \frac{3\sqrt{2}G_F m_{H/A} m_f^2 (\rho^f)^2}{8\pi} \times \begin{cases} \left(1 - \frac{4m_f^2}{m_H^2}\right)^{3/2}, & \text{H} \\ \left(1 - \frac{4m_f^2}{m_A^2}\right)^{1/2}, & \text{A} \end{cases}. \tag{16}$$

With equal Higgs boson masses and couplings, an additional factor of $1 - 4m_f^2/m_H^2$ in CP-even H decay with respect to the CP-odd A decay leads to suppression of $H \to t\bar{t}$ compared to $A \to t\bar{t}$ as can be seen in all model types. The consequence of this difference is that $A \to \tau\tau$ is less than $H \to \tau\tau$ above the kinematic threshold of decay to the top quark pair in type 4. This phenomenon is most relevant when $m_{H/A} \sim 2m_f$, otherwise the above term of $1 - 4m_f^2/m_{H/A}^2$ tends to unity and the difference between the rates of $H \to t\bar{t}$ and $A \to t\bar{t}$ becomes smaller as $m_{H/A}$ tends to 1 TeV.

In order to visualize the above statements and decide on analysis channels, the Higgs boson decay rates are obtained using 2HDMC 1.8.0 [98,99]. Since high $\tan\beta$ values are excluded in most model types, we start from $\tan\beta = 7$ and 10 inspired from the solutions of $m_t \cot\beta = m_b \tan\beta$ and $m_t \cot\beta = m_\tau \tan\beta$ to obtain open regions for analysis. These $\tan\beta$ values are turning points above which $H \to bb/\tau\tau$ in types 2, 3, and 4 start to overwhelm $H \to t\bar{t}$ when $m_{H/A} > 2m_t$. In type 4, the above argument is only valid for moderate masses up to 500 GeV while for heavier Higgs bosons, higher $\tan\beta$ values are needed to strengthen $H/A \to \tau\tau$. In type 1, regardless of $\tan\beta$, the dominant channel is $H \to t\bar{t}$ when kinematically allowed. Figures 3 and 4 show branching ratio of decays for both heavy neutral Higgs bosons in each type of the model at $\tan\beta = 7$ and 10. Based on these figures the following final states are considered for each type:

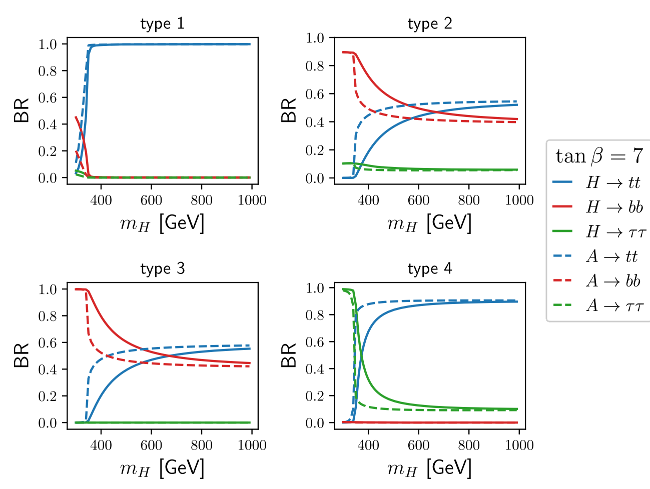

FIG. 3. Branching ratio of Higgs boson decays to the main channels at $\tan\beta = 7$. All heavy Higgs boson masses are assumed to be equal in this plot.

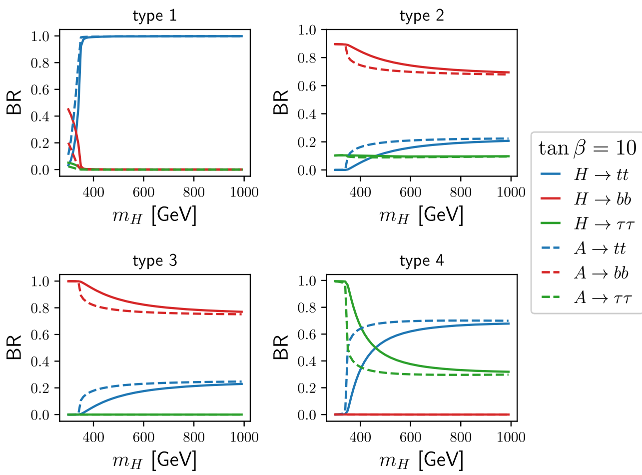

FIG. 4. The same as Fig. 3 but with $\tan\beta = 10$.

(i) *type 1*: $H/A \to b\bar{b}$ well below the top quark pair production threshold, i.e., $m_{H/A} < 2m_t$ and $H/A \to t\bar{t}$ near or above the threshold. Since the current analysis deals with $m_{H/A} \geq 300$ GeV, the latter is chosen.

(ii) *type 2*: This is actually highly suppressed by experimental searches for 2HDM and MSSM. A choice of $H/A \to b\bar{b}$ or $H/A \to \tau\tau$ is fine. If $H/A \to t\bar{t}$ is sizable (which is the case when $m_t \cot\beta \simeq m_b \tan\beta$), there is still preference in favor of $H/A \to b\bar{b}$ due to the lower final state particle multiplicity

(iii) *type 3*: $H/A \to b\bar{b}$ is dominant as long as high $\tan\beta$ values are considered. The same argument as in type 2 is applied to $H/A \to t\bar{t}$.

(iv) *type 4*: $H/A \to \tau\tau$ is dominant as long as high $\tan\beta$ values are considered. In this case also $H/A \to t\bar{t}$ can be sizable (when $m_t \cot\beta \simeq m_\tau \tan\beta$). However, due to the same reasons as mentioned in type 2, $H/A \to \tau\tau$ is preferred.

The experimental exclusion regions are obtained using HiggsTools-1 [100] which is a collection of HiggsBounds-6 [101–105], HiggsSignals-3 [106–108], and the new code HiggsPredictions-1. At the moment, results of 258 analyses from LEP to LHC are included in the code database. The input data for obtaining excluded regions are the scaled effective Higgs-fermion and Higgs-gauge couplings relative to SM and the Higgs boson decay rates for nonfermionic channels like $H \to hh$ and $A \to ZH$ which are taken (borrowed) from 2HDMC.

Figures 5 and 6 show the resulting excluded regions for $\tan\beta = 7$ and 10 together with the signal cross section times branching ratio of decay to the relevant final state in each type. The red line indicates the border of two scenarios of the collider operation at $\sqrt{s} = 1400$ and 3000 GeV. The excluded regions in type 1 (at $\tan\beta = 7$) and type 3 at $m_H < 400$ GeV refer to the LHC analysis of the Higgs boson conversion reported in [109]. In type 3, at $\tan\beta = 10$ there are two points of $(m_H, m_A) = (470, 490)$ and (490, 470) GeV excluded by LHC [110]. The type 2 is

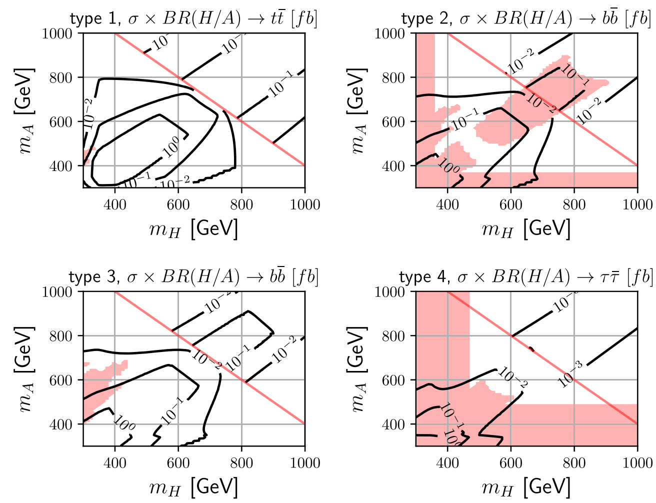

FIG. 5. The signal cross section times branching ratio of decay to relevant final states in each type at $\tan\beta = 7$. The current excluded regions at 95% CL are shown in solid red.

excluded mainly by the two LHC analyses reported in [109,111]. The type 4 excluded regions refer to [111] and [112,113]. In types 3 and 4, the higher the $\tan\beta$, the more signal sensitivity due to the higher branching ratio of Higgs boson decay. Therefore $\tan\beta = 10$ is chosen for the rest of the analysis. At this value, type 2 is already excluded up to near 1 TeV. The LHC exclusion of type 2 parameter space is in agreement with the prediction reported in [114] where it was shown that MSSM Higgs boson masses up to 1 TeV at $\tan\beta = 10$ can be excluded at HL-LHC integrated luminosity of 300 fb^{-1}. Higher masses up to several TeV were analyzed in [115] for a hadron collider operating at 100 TeV (FCC-hh). These results and current LHC experimental results shown in Figs. 5 and 6 (based on [109–113])

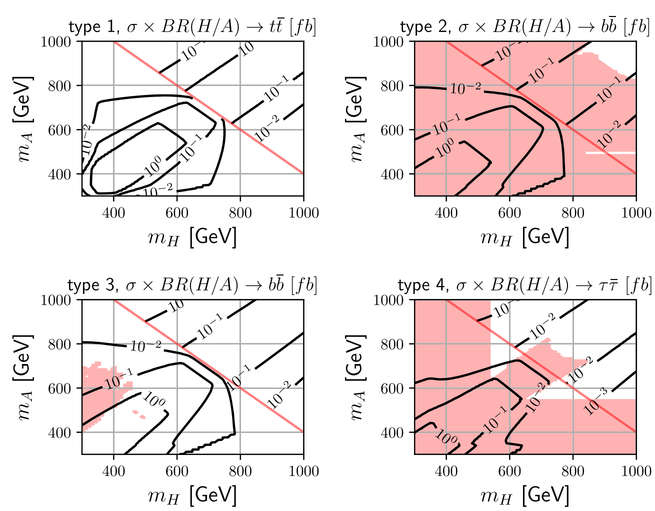

FIG. 6. The signal cross section times branching ratios with the same descriptions as in Fig. 5 but with $\tan\beta = 10$.

show that the current open regions of the parameter space are reasonable choices for CLIC studies.

IV. SIGNAL AND BACKGROUND GENERATION

The main background events are electroweak boson pair production ZZ (including γ) and top quark pair production $t\bar{t}$. The single boson production (Drell-Yan) does not contribute as it contains fewer jets needed to fully reconstruct events. The W^+W^- background contribution is also negligible due to the presence of the light jets in the final state and low fake rate.

Both signal and background processes are generated starting from WHIZARD which produces LHEF files containing the hard scattering [116]. These files are used by PYTHIA 8.3.09 [117] which is called through DELPHES [118–120] for fast detector simulation. The jet reconstruction is performed using the Valencia algorithm [121] as proposed by the CLIC Collaboration [122] due to its robust performance in the non-negligible background environment, which is even better than the k_T algorithm [123].

The WHIZARD package performs bremsstrahlung and initial state radiation from the beam particles using CIRCE2 code [124] resulting in the beam spectrum as shown in Fig. 7. The bremsstrahlung not only reduces the beam energy but also results in radiated photon collisions as the so-called overlay background [125]. These events have been shown to be reducing the jet energy resolution in preliminary studies and their effects are minimally included as a source of jet energy smearing applied after the jet reconstruction by DELPHES. The values implemented for the two scenarios of 1400 and 3000 GeV are shown in Table II where pseudorapidity is defined as $\eta = -\ln \tan \theta/2$ (θ is the polar angle with respect to the beam axis).

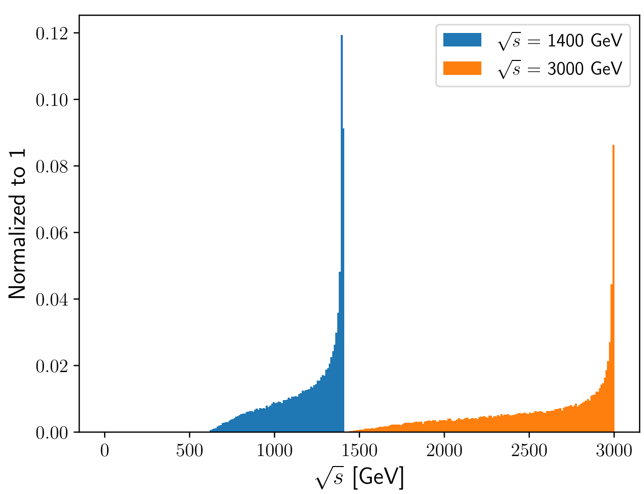

FIG. 7. Beam spectrum at $\sqrt{s} = 1400$ and 3000 GeV, simulated by CIRCE2 and used for event generation by WHIZARD.

TABLE II. The jet energy smearing in percent applied on jets in the two regions of pseudorapidity to mimic the $\gamma\gamma \to$ hadrons overlay background.

$\sqrt{s}$ (GeV)	1400	3000
$\lvert\eta\rvert < 0.76$	1%	2%
$\lvert\eta\rvert \geq 0.76$	5%	10%

V. BENCHMARK POINTS

Figure 6 shows that the signal rates are higher around the diagonal line of degenerate masses due to the cross section symmetry. Therefore, the set of benchmark points for the analysis are divided into two categories of degenerate and nondegenerate masses. The set of $m_H = m_A$ points are chosen with increments of 100 GeV starting from 300 to 600 GeV for collider operation at $\sqrt{s} = 1400$ GeV and 700 to 1000 GeV for the scenario of $\sqrt{s} = 3000$ GeV. The nondegenerate points are chosen with the same CP-even heavy Higgs boson masses but with $m_A = m_H + 50$ GeV for the two center of mass energies. These points are relevant to types 1 and 3. In type 4, m_H starts from 800 GeV as lower masses are already excluded.

The Z_2 soft breaking mass parameter m_{12} is set through the relation $m_{12}^2 = m_H^2 \sin\beta \cos\beta$ which is suggested in [126] as a consequence of natural SM alignment of the model without requiring the decoupling or a fine-tuning. For completeness, we recall other parameters of the model: $\tan\beta = 10$ and $\sin(\beta - \alpha) = 1$.

Tables III and IV show the signal and background cross sections as a numeric reference. It should be noted that the background processes are generated in a fully hadronic final state to reduce the statistics. Therefore, ZZ and $t\bar{t}$

TABLE III. Signal cross section at benchmark points. Higgs boson masses are in GeV.

$\sqrt{s}$ (GeV)	Higgs boson masses and cross sections				
1400	$m_H = m_A =$	300	400	500	600
	σ(fb)	4.8	2.8	1.3	0.37
	$m_A = m_H + 50 =$	350	450	550	650
	σ(fb)	4.3	2.4	1.1	0.22
3000	$m_H = m_A =$	700	800	900	1000
	σ(fb)	0.84	0.64	0.48	0.34
	$m_A = m_H + 50 =$	750	850	950	1050
	σ(fb)	0.79	0.6	0.44	0.31

TABLE IV. Background cross sections.

$\sqrt{s}$ (GeV)		ZZ	$t\bar{t}$	hZ
1400	σ(fb)	142	145	13.5
3000	σ(fb)	58	53	4.7

backgrounds undergo $Z \to q\bar{q}$ and $W \to q\overline{q'}$, respectively, with branching ratios of 0.69 and 0.68 [93]. The hZ process is also analyzed in the four b-jet final state in type 3 with $\mathrm{BR}(h \to b\bar{b}) = 0.55$. In type 4, this background has no sizable contribution in the signal region.

VI. ANALYSIS, TYPE 1

The type 1 events are predominantly in the four top quark final state above the kinematic threshold. Events are therefore produced with high particle multiplicity if top quarks decay hadronically. With a normal cone size of 0.5 one would expect to have three jets from each top quark in its fully hadronic final state resulting in a total of 12 jets. In this case the top tagging algorithm [127–130] can be used to identify the highly boosted top quarks based on the jet substructure [131–134]. There are several top tagging algorithms, two of which are used in this analysis, namely, HEPTopTagger2 [135,136] and JohnHopkins [137]. The external codes for these algorithms are linked to the FastJetFinder jet reconstruction module inside DELPHES. The performance of the algorithm is expected to increase with increasing Higgs boson masses thus producing highly boosted top quarks. The jet reconstruction cone is set to 0.8 with the Cambridge-Aachen algorithm used for the jet reconstruction [138]. This choice of the jet cone gives, on average, four identified jets to be used as input by the top tagging algorithm.

The identified top jets from Higgs bosons with $m_H = m_A = 700$ GeV at $\sqrt{s} = 3000$ GeV result in the multiplicity distribution as shown in Fig. 8. As seen, the jet multiplicity has a peak at four, while identified top jets have no sizable contribution in the four top bins for both algorithms. Therefore, with the choice of the top tagging algorithms examined here, the signal cannot be reconstructed unless a detailed study of this type with more sophisticated top tagging algorithms based on machine learning is performed.

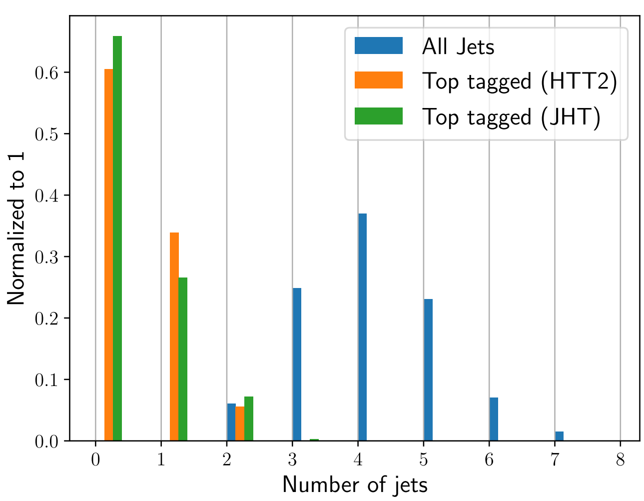

FIG. 8. Number of identified top jets in the signal events at $\sqrt{s} = 3000$ GeV using two top tagging algorithms, HEPTopTagger2 (labeled HTT2) and JohnHopkins (labeled JHT).

TABLE V. Branching ratio of CP-even and CP-odd Higgs boson decay to $b\bar{b}$ in types 2 and 3 for the two points outside the current excluded area.

Higgs Boson Masses	Model	Channels	
$m_{H/A} = 500$ GeV		$H \to b\bar{b}$	$A \to b\bar{b}$
	Type 2	0.49	0.36
	Type 3	0.53	0.39
$m_{H/A} = 900$ GeV		$H \to b\bar{b}$	$A \to b\bar{b}$
	Type 2	0.35	0.33
	Type 3	0.38	0.35

VII. ANALYSIS, TYPE 2

Although type 2 is very limited at $\tan\beta = 10$, which is the base for the analysis, one point worthy to mention is that the signal topology and kinematics of the final state make no difference between types 2 and 3 with the same Higgs boson masses and decay channels. Therefore, taking into account branching ratio of Higgs boson decays in two types, the signal sensitivity in type 3 can easily be normalized to get the corresponding results in type 2.

As an example, at $\tan\beta = 7$, two scenarios of $m_H = m_A = 500$ GeV and $m_H = m_A = 900$ GeV, which are not yet excluded, lead to the following BRs for the four b-jet final state as shown in Table V. Because of the similarity of figures, one would expect to get similar results in type 2 by translating an analysis in the same final state in type 3.

VIII. ANALYSIS, TYPE 3

The type 3 events are analyzed in the four b-jet final state using the b-tagging algorithm optimized for the CLIC detector environment [139]. The kinematic acceptance for the jet reconstruction is $p_T > 10$ GeV and $|\eta| < 2$. The ZZ background shows less efficiency of four jet reconstruction compared to other backgrounds due to the electroweak nature of these events and wide pseudorapidity distribution of the jets as shown in Fig. 9. The kinematic acceptance has, therefore, lower efficiency of selection at higher center of mass energies for this background.

There are three scenarios of b-tagging with the efficiencies of 90%, 70%, and 50% including a fake rate from gluons and c-jets as a function of the jet energy and pseudorapidity. These working points are examined for the main background samples, $t\bar{t}$, ZZ, and hZ with the reconstructed jet multiplicities as well as those of b-jets shown in Figs. 10–12.

The lower b-tagging efficiency, the higher suppression of the background. However, even the loose b-tagging

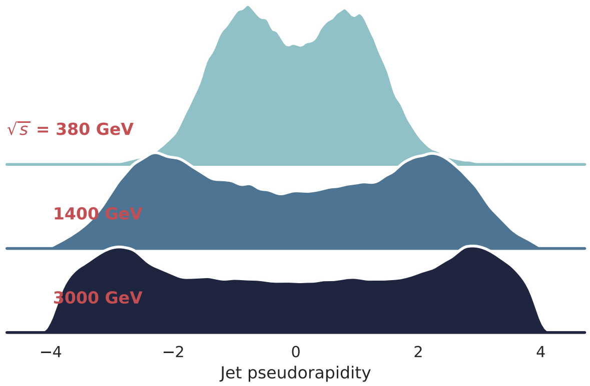

FIG. 9. The jet pseudorapidity distribution in the ZZ background as a function of the collider center of mass energy.

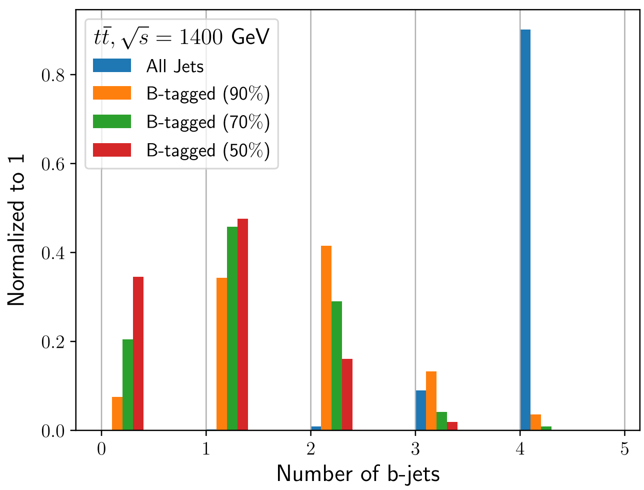

FIG. 10. Number of identified b-jets with different b-tagging efficiencies in $t\bar{t}$ events at $\sqrt{s} = 1400$ GeV.

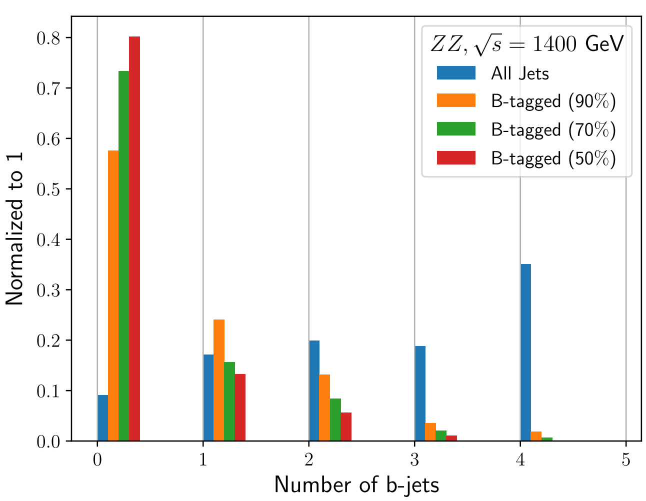

FIG. 11. Number of identified b-jets with different b-tagging efficiencies in ZZ events at $\sqrt{s} = 1400$ GeV.

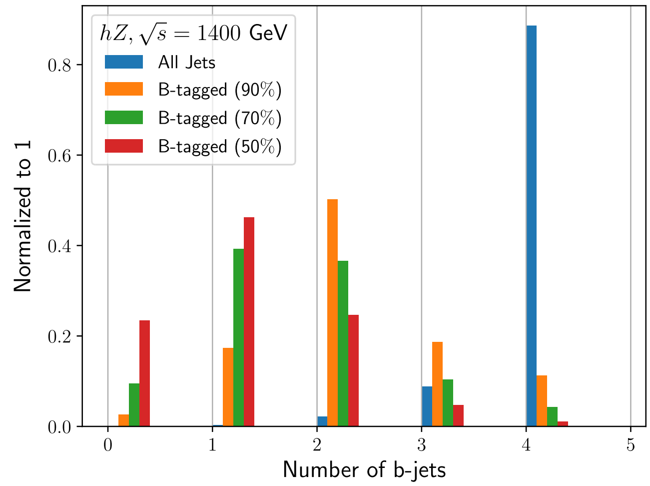

FIG. 12. Number of identified b-jets with different b-tagging efficiencies in hZ events at $\sqrt{s} = 1400$ GeV.

scenario with 90% efficiency allows a very small fraction of background events to fill the four b-jet bin and is thus chosen for the rest of the analysis.

In the next step, a kinematic fit is applied by imposing energy and momentum conservation on events with four reconstructed b-jets as proposed in the LEP (ALEPH) analysis [140]. The idea is to apply correction factors to the b-jets so that the set of four-momentum conservation equations [Eq. (17)] are satisfied:

$$\sum_{j=1}^{4} c_j \vec{p}_j = 0$$
$$\sum_{j=1}^{4} c_j E_j = \sqrt{s} \tag{17}$$

Despite the uncertainty in the center of mass energy due to the beam spectrum, correction factors yield reasonable results as will be seen soon. Figure 13 shows the distribution of the correction factors c_j with their average values close to (but slightly above) unity for an example benchmark point of $m_H = m_A = 300$ GeV at $\sqrt{s} = 1400$ GeV.

The b-jets are sorted in terms of their energies before correction. The wider distributions for softer jets are due to the more uncertainty in the jet reconstruction with lower energy. Since all four-momentum components of each b-jet is to be multiplied by the corresponding correction factor, we require that all c_j with $j = 1$ to 4 are positive to avoid negative energies after correction. The energy sorting is repeated after correction and b-jets are labeled as b_i with $i = 1$ to 4 denoting the hardest to the softest b-jet in the list.

In the next step, b-jet pairing is performed as described in [69] using invariant masses of b_2b_3 and b_1b_4 together in one histogram. Although b_2b_3 pairs have proved to result in better invariant mass distributions for the Higgs bosons, the

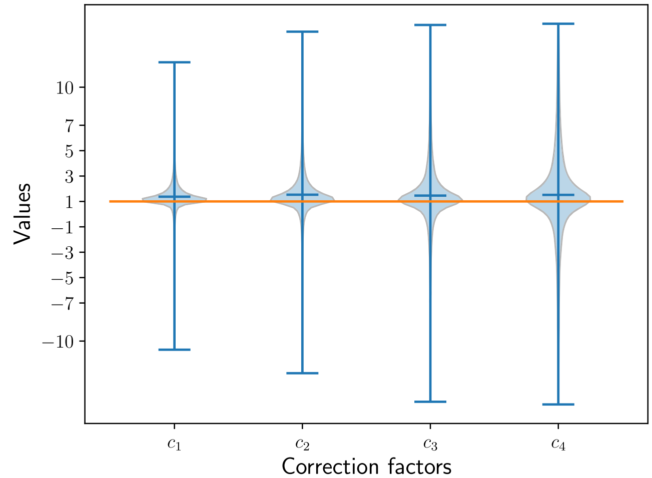

FIG. 13. Distribution of the correction factors obtained by solving Eq. (17).

two pairs are used to get double statistics. Figures 14(a) (equal masses) and 14(b) (different masses) show the reconstructed Higgs boson invariant masses on top of the background at $\sqrt{s} = 1400$ GeV. Results of higher masses at $\sqrt{s} = 3000$ GeV are shown in Figs. 15(a) and 15(b). Signals are stacked on the background but not on each other. As seen from Figs. 14(b) and 15(b) the two Higgs bosons can be distinguished if their masses are different.

In obtaining these distributions, the charged track momentum smearing and ECAL/HCAL energy resolution are included using the standard CLIC detector card implemented in DELPHES.

A mass window optimization is performed to get the highest signal significance, $S/\sqrt{B}$, and values exceeding 5σ are obtained in all benchmark points at integrated luminosity of 1000 fb^{-1}. Therefore, final results are presented in terms of the integrated luminosity needed for 5σ discovery as shown in Fig. 16. The lowest signal sensitivity for $m_H = 600$ GeV is due to $m_H + m_A$ getting close to the center of mass energy thus saturating the phase space. As a result, the cross section is small and more data is needed for the signal observation.

IX. ANALYSIS, TYPE 4

Type 4 prefers leptonic decays of the Higgs bosons with Higgs-fermion couplings proportional to $\tan\beta$. At $\tan\beta = 10$, $m_t \cot\beta \sim m_\tau \tan\beta$ and the two decay modes compete. The $A \to \tau\tau$ is slightly smaller than $H \to \tau\tau$ due to what was said in Eq. (16). At higher $\tan\beta$, $H/A \to \tau\tau$ supersedes $H/A \to t\bar{t}$ and the signal rate is higher. Therefore we take $\tan\beta = 10$ as the bottom line above which higher S/B is expected.

The τ-tagging algorithm in the hadronic final state is performed with efficiencies depending on p_T and η of the τ-jet. The fake rate is assumed to be 3% with the τ-tagging efficiency around 60% for $p_T > 50$ GeV [141].

As seen from Fig. 6, the Higgs boson masses below 800 GeV are already excluded in type 4 at $\tan\beta = 10$; therefore, three scenarios of $m_H = m_A = 800$, 900, 1000 GeV and $m_A = m_H + 50 = 850$, 950, 1050 GeV are examined in the four τ-jet final state. The kinematic selection and procedure for τ-jet pairing is the same as what was described in the previous section. There is small background left in the signal region in this case and the

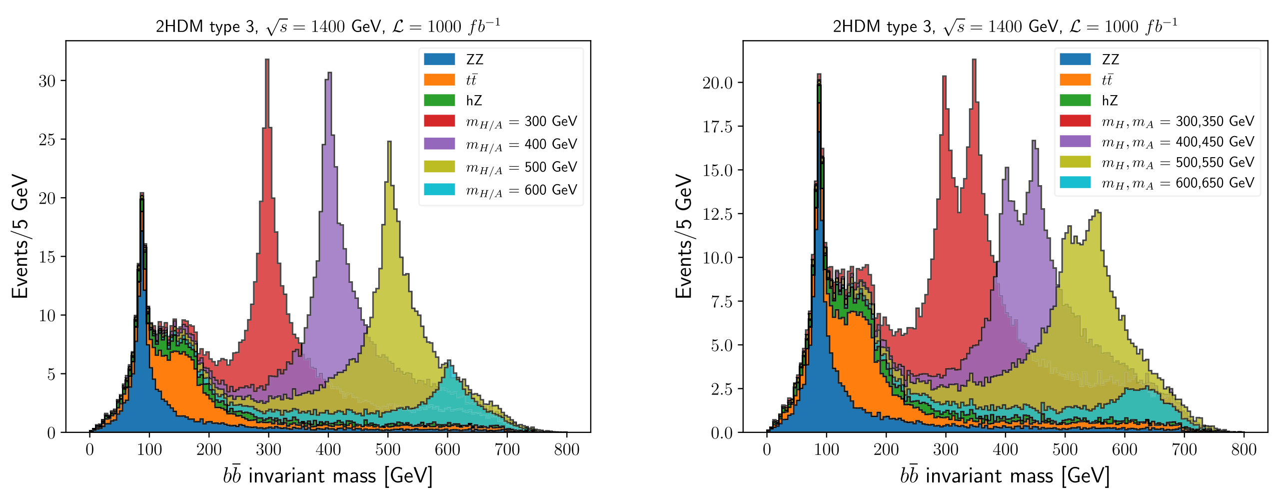

(a) Equal masses (b) Different masses

FIG. 14. The b-jet pair invariant mass distributions in signal and background events for type 3 with $\sqrt{s} = 1400$ GeV. The signals containing $m_H = m_A = 300$ and 400 GeV are divided by 5 and 2 and those with $m_A = m_H + 50 = 350$ and 450 are divided by 3 and 2 to fit the window.

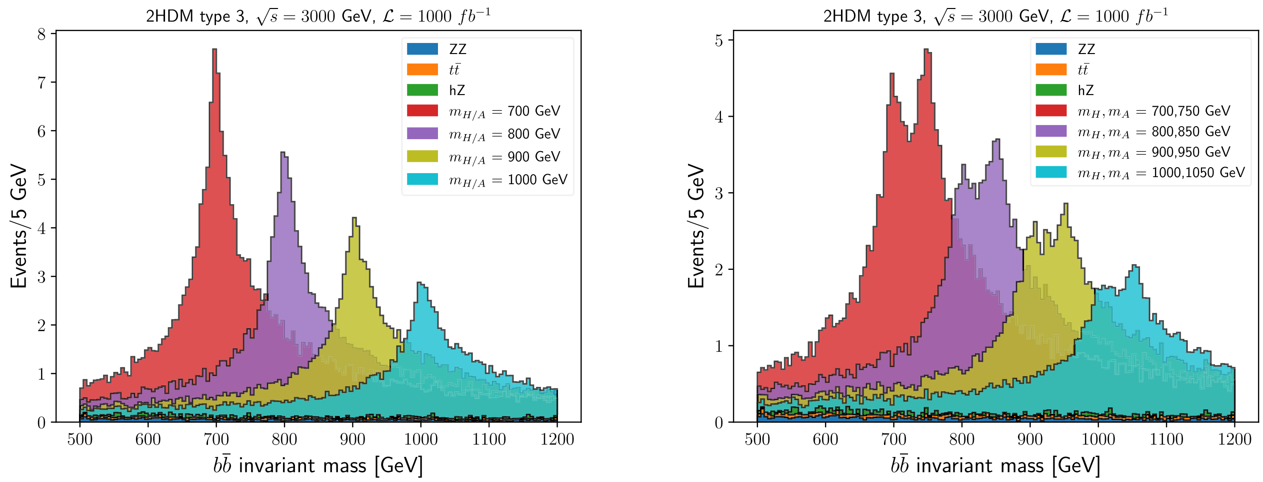

(a) Equal masses (b) Different masses

FIG. 15. The b-jet pair invariant mass distributions in signal and background events for type 3 with $\sqrt{s} = 3000$ GeV.

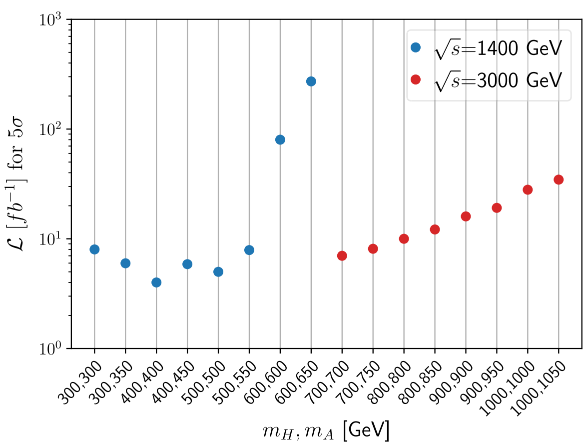

FIG. 16. Integrated luminosity $\mathcal{L}$ needed for 5σ discovery in 2HDM type 3.

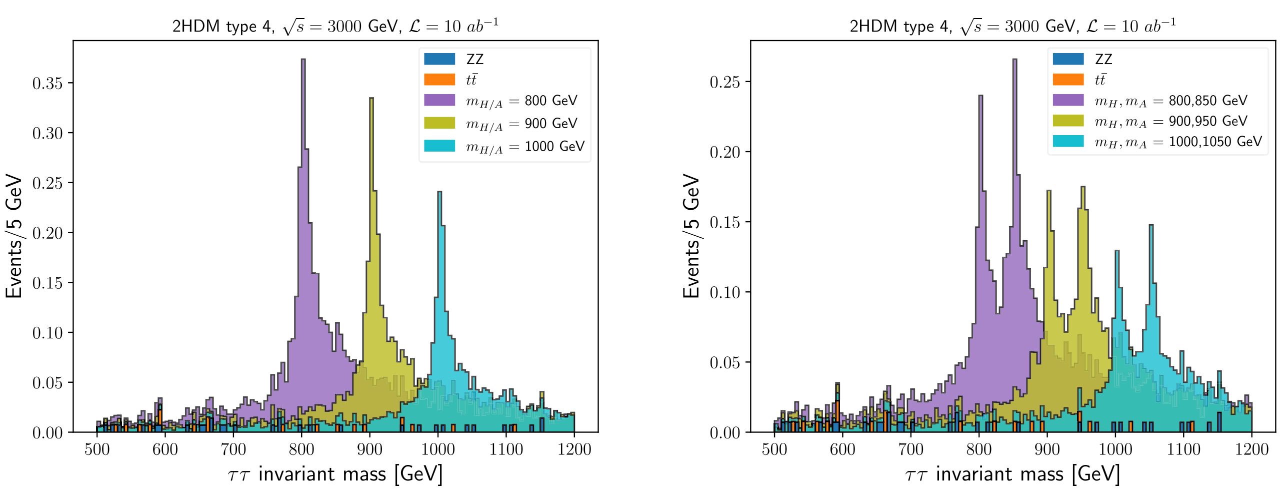

(a) Equal masses (b) Different masses

FIG. 17. The τ-jet pair invariant mass distributions in signal and background events for type 4 with $\sqrt{s} = 3000$ GeV.

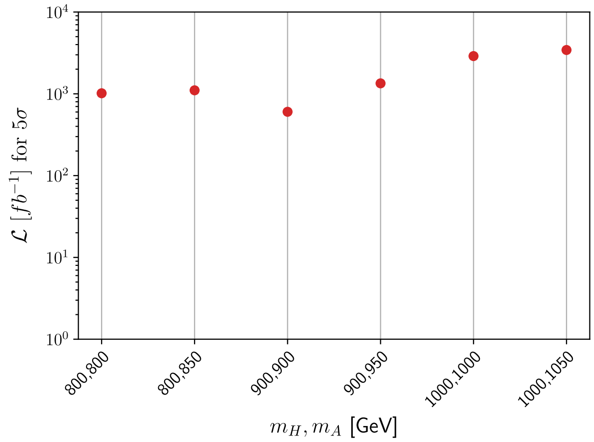

FIG. 18. Integrated luminosity $\mathcal{L}$ needed for 5σ discovery in 2HDM type 4.

signal lies on an almost background free region as shown in Figs. 17(a) and 17(b).

The signal distributions are sharper than the case of four b-jet final state in type 3. However, due to the lower signal rate and τ tagging efficiencies, more data or integrated luminosity are needed for the 5σ discovery compared to the case of type 3. Figure 18 shows the integrated luminosity in fb^{-1} needed for 5σ discovery.

X. CONCLUSIONS

The heavy neutral 2HDM Higgs boson pair production was studied in the mass range of 300 to 1000 GeV at two stages of the CLIC operation, i.e., $\sqrt{s} = 1400$ and 3000 GeV. The signal was analyzed in the relevant final states of each 2HDM type in the regions of the parameter space not yet excluded by the current LHC 8 and 13 TeV analyses.

Type 1, with its dominant final state of four top quarks, shows poor top tagging performance with the two exploited algorithms. A more sophisticated analysis using machine learning algorithms is needed to obtain a reasonable signal in this type. While type 2 with its similar decay rates to type 3 at $\tan\beta \simeq 10$ is almost fully excluded, type 3 shows a promising signal on top of the background with distinct signals for CP-even and CP-odd Higgs bosons in scenarios with different masses. Type 4 shows a sharper but with less statistics at high masses above 800 GeV which will be accessible at $\sqrt{s} = 3000$ GeV. Overall results show that the signal observation is possible at integrated luminosities below 1000 fb^{-1} in type 3, and 10 ab^{-1} in type 4 in the mass ranges under study within the limits of the analysis performed in this work. A more detailed study with possibly full detector simulation and more realistic collider environment is needed for the final conclusions.

[1] P. W. Higgs, Phys. Rev. Lett. **13**, 508 (1964).
[2] P. W. Higgs, Phys. Lett. **12**, 132 (1964).
[3] P. W. Higgs, Phys. Rev. **145**, 1156 (1966).
[4] F. Englert and R. Brout, Phys. Rev. Lett. **13**, 321 (1964).
[5] G. S. Guralnik, C. R. Hagen, and T. W. B. Kibble, Phys. Rev. Lett. **13**, 585 (1964).
[6] T. W. B. Kibble, Phys. Rev. **155**, 1554 (1967).
[7] G. Aad *et al.* (ATLAS Collaboration), Phys. Lett. B **716**, 1 (2012).
[8] S. Chatrchyan *et al.* (CMS Collaboration), Phys. Lett. B **716**, 30 (2012).
[9] A. M. Sirunyan *et al.* (CMS Collaboration), Phys. Lett. B **792**, 369 (2019).
[10] A. M. Sirunyan *et al.* (CMS Collaboration), Eur. Phys. J. C **79**, 421 (2019).
[11] A. M. Sirunyan *et al.* (CMS Collaboration), Phys. Rev. Lett. **125**, 061801 (2020).
[12] G. Aad *et al.* (ATLAS and CMS Collaborations), J. High Energy Phys. 08 (2016) 045.
[13] G. Aad *et al.* (ATLAS Collaboration), Phys. Rev. D **101**, 012002 (2020).
[14] G. Aad *et al.* (ATLAS Collaboration), Phys. Rev. Lett. **125**, 061802 (2020).
[15] G. Aad *et al.* (ATLAS Collaboration), Phys. Lett. B **805**, 135426 (2020).
[16] G. Aad *et al.* (ATLAS Collaboration), Eur. Phys. J. C **75**, 476 (2015); **76**, 152(E) (2016).
[17] M. Dine and A. Kusenko, Rev. Mod. Phys. **76**, 1 (2003).
[18] O. Buchmueller, M. Citron, J. Ellis, S. Guha, J. Marrouche, K. A. Olive, K. de Vries, and J. Zheng, Eur. Phys. J. C **75**, 469 (2015); **76**, 190(E) (2016).
[19] S. A. Malik *et al.*, Phys. Dark Universe **9–10**, 51 (2015).
[20] I. B. Logashenko and S. I. Eidelman, Phys. Usp. **61**, 480 (2018).
[21] S. P. Martin, Adv. Ser. Dir. High Energy Phys. **18**, 1 (1998).
[22] I. J. R. Aitchison, arXiv:hep-ph/0505105.
[23] M. Carena and H. E. Haber, Prog. Part. Nucl. Phys. **50**, 63 (2003).
[24] H. Haber and G. Kane, Phys. Rep. **117**, 75 (1985).
[25] E. Ma and D. Ng, Phys. Rev. D **49**, 6164 (1994).
[26] A. Djouadi, Phys. Rep. **459**, 1 (2008).
[27] T. D. Lee, Phys. Rev. D **8**, 1226 (1973).
[28] S. L. Glashow and S. Weinberg, Phys. Rev. D **15**, 1958 (1977).
[29] G. C. Branco, Phys. Rev. D **22**, 2901 (1980).
[30] M. Misiak *et al.*, Phys. Rev. Lett. **114**, 221801 (2015).
[31] F. Mahmoudi and O. Stal, Phys. Rev. D **81**, 035016 (2010).
[32] T. Aaltonen *et al.* (CDF Collaboration), Science **376**, 170 (2022).

[33] S. Davidson and H. E. Haber, Phys. Rev. D **72**, 035004 (2005); **72**, 099902(E) (2005).
[34] M. Aoki, S. Kanemura, K. Tsumura, and K. Yagyu, Phys. Rev. D **80**, 015017 (2009).
[35] J. Bernon, J. F. Gunion, H. E. Haber, Y. Jiang, and S. Kraml, Phys. Rev. D **92**, 075004 (2015).
[36] J. Bernon, J. F. Gunion, H. E. Haber, Y. Jiang, and S. Kraml, Phys. Rev. D **93**, 035027 (2016).
[37] B. Grzadkowski, H. E. Haber, O. M. Ogreid, and P. Osland, J. High Energy Phys. 12 (2018) 056.
[38] A. M. Sirunyan *et al.* (CMS Collaboration), J. High Energy Phys. 03 (2020) 055.
[39] H. E. Haber and D. O'Neil, Phys. Rev. D **74**, 015018 (2006); **74**, 059905(E) (2006).
[40] A. M. Sirunyan *et al.* (CMS Collaboration), J. High Energy Phys. 01 (2018) 054.
[41] A. M. Sirunyan *et al.* (CMS Collaboration), Phys. Lett. B **778**, 101 (2018).
[42] A. M. Sirumyan *et al.* (CMS Collaboration), J. High Energy Phys. 08 (2018) 152.
[43] A. M. Sirunyan *et al.* (CMS Collaboration), Phys. Lett. B **781**, 244 (2018).
[44] A. M. Sirunyan *et al.* (CMS Collaboration), Phys. Rev. D **102**, 032003 (2020).
[45] ATLAS Collaboration, Report No. ATLAS-CONF-2016-004, ATLAS-CONF-2016-004, 2016.
[46] ATLAS Collaboration, Report No. ATLAS-CONF-2016-071, 2016.
[47] ATLAS Collaboration, Report No. ATLAS-CONF-2016-049, 2016.
[48] M. Aaboud *et al.* (ATLAS Collaboration), J. High Energy Phys. 01 (2019) 030.
[49] A. M. Sirunyan *et al.* (CMS Collaboration), Eur. Phys. J. C **79**, 564 (2019).
[50] V. Khachatryan *et al.* (CMS Collaboration), Phys. Lett. B **755**, 217 (2016).
[51] H. Y.-s. Tong, Master's thesis, Taiwan, Natl. Central U., 2016.
[52] M. Aaboud *et al.* (ATLAS Collaboration), Phys. Lett. B **783**, 392 (2018).
[53] G. Aad *et al.* (ATLAS Collaboration), Eur. Phys. J. C **81**, 396 (2021).
[54] G. Aad *et al.* (ATLAS Collaboration), Phys. Lett. B **744**, 163 (2015).
[55] W. Grimus, L. Lavoura, O. M. Ogreid, and P. Osland, J. Phys. G **35**, 075001 (2008).
[56] J.-M. Gérard and M. Herquet, Phys. Rev. Lett. **98**, 251802 (2007).
[57] S. Bertolini, Nucl. Phys. **B272**, 77 (1986).
[58] A. Denner, R. Guth, and J. Kühn, Phys. Lett. B **240**, 438 (1990).
[59] M. Cepeda *et al.*, CERN Yellow Rep. Monogr. **7**, 221 (2019).
[60] H. Bahl, P. Bechtle, S. Heinemeyer, S. Liebler, T. Stefaniak, and G. Weiglein, Eur. Phys. J. C **80**, 916 (2020).
[61] H. Abramowicz *et al.*, Eur. Phys. J. C **77**, 475 (2017).
[62] E. Sicking, Nucl. Part. Phys. Proc. **273–275**, 801 (2016).
[63] D. M. Asner *et al.*, in Community Summer Study 2013: Snowmass on the Mississippi (2013), arXiv:1310.0763.
[64] D. d'Enterria, Proc. Sci., ICHEP2016 (**2017**) 434.
[65] F. An *et al.*, Chin. Phys. C **43**, 043002 (2019).
[66] M. Hashemi and G. Haghighat, Eur. Phys. J. C **79**, 419 (2019).
[67] M. Hashemi and G. Haghighat, Nucl. Phys. **B951**, 114903 (2020).
[68] M. Hashemi and G. Haghighat, J. Phys. G **45**, 095005 (2018).
[69] M. Hashemi and E. Ebrahimi, Phys. Rev. D **103**, 115008 (2021).
[70] M. Hashemi and G. Haghighat, Phys. Rev. D **100**, 015047 (2019).
[71] M. Hashemi and N. N. Ghalati, Phys. Lett. B **830**, 137153 (2022).
[72] M. Hashemi, Phys. Rev. D **98**, 115004 (2018).
[73] M. Hashemi, Eur. Phys. J. C **77**, 302 (2017).
[74] M. Hashemi and G. Haghighat, Phys. Lett. B **772**, 426 (2017).
[75] J. McDonald, Phys. Rev. D **50**, 3637 (1994).
[76] C. P. Burgess, M. Pospelov, and T. ter Veldhuis, Nucl. Phys. **B619**, 709 (2001).
[77] D. O'Connell, M. J. Ramsey-Musolf, and M. B. Wise, Phys. Rev. D **75**, 037701 (2007).
[78] O. Bahat-Treidel, Y. Grossman, and Y. Rozen, J. High Energy Phys. 05 (2007) 022.
[79] V. Barger, P. Langacker, M. McCaskey, M. J. Ramsey-Musolf, and G. Shaughnessy, Phys. Rev. D **77**, 035005 (2008).
[80] X.-G. He, T. Li, X.-Q. Li, and H.-C. Tsai, Mod. Phys. Lett. A **22**, 2121 (2007).
[81] H. Davoudiasl, R. Kitano, T. Li, and H. Murayama, Phys. Lett. B **609**, 117 (2005).
[82] V. Barger, P. Langacker, M. McCaskey, M. Ramsey-Musolf, and G. Shaughnessy, Phys. Rev. D **79**, 015018 (2009).
[83] R. Coimbra, M. O. P. Sampaio, and R. Santos, Eur. Phys. J. C **73**, 2428 (2013).
[84] R. Costa, A. P. Morais, M. O. P. Sampaio, and R. Santos, in *2nd Toyama International Workshop on Higgs as a Probe of New Physics* (2015), arXiv:1504.06421.
[85] M. Gonderinger, H. Lim, and M. J. Ramsey-Musolf, Phys. Rev. D **86**, 043511 (2012).
[86] G.-C. Cho, C. Idegawa, and R. Sugihara, Phys. Lett. B **839**, 137757 (2023).
[87] L. Lopez Honorez, E. Nezri, J. F. Oliver, and M. H. G. Tytgat, J. Cosmol. Astropart. Phys. 02 (2007) 028.
[88] M. H. G. Tytgat, J. Phys. Conf. Ser. **120**, 042026 (2008).
[89] A. Ilnicka, M. Krawczyk, and T. Robens, Phys. Rev. D **93**, 055026 (2016).
[90] A. Goudelis, B. Herrmann, and O. Stål, J. High Energy Phys. 09 (2013) 106.
[91] E. Lundstrom, M. Gustafsson, and J. Edsjo, Phys. Rev. D **79**, 035013 (2009).
[92] C. Bonilla, D. Sokolowska, N. Darvishi, J. L. Diaz-Cruz, and M. Krawczyk, J. Phys. G **43**, 065001 (2016).
[93] K. A. Olive *et al.* (Particle Data Group), Chin. Phys. C **38**, 090001 (2014).
[94] W. Kilian, T. Ohl, and J. Reuter, Eur. Phys. J. C **71**, 1742 (2011).

[95] M. Moretti, T. Ohl, and J. Reuter, arXiv:hep-ph/0102195.
[96] L. R. Surguladze, Phys. Lett. B **341**, 60 (1994).
[97] L. R. Surguladze, Phys. Lett. B **338**, 229 (1994).
[98] D. Eriksson, J. Rathsman, and O. Stal, Comput. Phys. Commun. **181**, 189 (2010).
[99] D. Eriksson, J. Rathsman, and O. Stal, Comput. Phys. Commun. **181**, 833 (2010).
[100] H. Bahl, T. Biekötter, S. Heinemeyer, C. Li, S. Paasch, G. Weiglein, and J. Wittbrodt, Comput. Phys. Commun. **291**, 108803 (2023).
[101] P. Bechtle, O. Brein, S. Heinemeyer, G. Weiglein, and K. E. Williams, Comput. Phys. Commun. **181**, 138 (2010).
[102] P. Bechtle, O. Brein, S. Heinemeyer, G. Weiglein, and K. E. Williams, Comput. Phys. Commun. **182**, 2605 (2011).
[103] P. Bechtle, O. Brein, S. Heinemeyer, O. Stal, T. Stefaniak, G. Weiglein, and K. Williams, Proc. Sci., CHARGED2012 (**2012**) 024.
[104] P. Bechtle, O. Brein, S. Heinemeyer, O. Stål, T. Stefaniak, G. Weiglein, and K. E. Williams, Eur. Phys. J. C **74**, 2693 (2014).
[105] P. Bechtle, S. Heinemeyer, O. Stal, T. Stefaniak, and G. Weiglein, Eur. Phys. J. C **75**, 421 (2015).
[106] P. Bechtle, S. Heinemeyer, O. Stål, T. Stefaniak, and G. Weiglein, Eur. Phys. J. C **74**, 2711 (2014).
[107] O. Stål and T. Stefaniak, Proc. Sci., EPS-HEP2013 (**2013**) 314.
[108] P. Bechtle, S. Heinemeyer, O. Stål, T. Stefaniak, and G. Weiglein, J. High Energy Phys. 11 (2014) 039.
[109] M. Aaboud *et al.* (ATLAS Collaboration), Phys. Lett. B **783**, 392 (2018).
[110] M. Aaboud *et al.* (ATLAS Collaboration), Phys. Lett. B **795**, 56 (2019).
[111] G. Aad *et al.* (ATLAS Collaboration), Phys. Rev. Lett. **125**, 051801 (2020).
[112] CMS Collaboration, J. High Energy Phys. 07 (2023) 073.
[113] V. Khachatryan *et al.* (CMS Collaboration), Phys. Lett. B **759**, 369 (2016).
[114] A. Djouadi, L. Maiani, A. Polosa, J. Quevillon, and V. Riquer, J. High Energy Phys. 06 (2015) 168.
[115] J. Baglio, A. Djouadi, and J. Quevillon, Rep. Prog. Phys. **79**, 116201 (2016).
[116] J. Alwall *et al.*, Comput. Phys. Commun. **176**, 300 (2007).
[117] T. Sjostrand, S. Mrenna, and P. Z. Skands, Comput. Phys. Commun. **178**, 852 (2008).
[118] J. de Favereau, C. Delaere, P. Demin, A. Giammanco, V. Lemaître, A. Mertens, and M. Selvaggi (DELPHES 3 Collaboration), J. High Energy Phys. 02 (2014) 057.
[119] M. Selvaggi, J. Phys. Conf. Ser. **523**, 012033 (2014).
[120] A. Mertens, J. Phys. Conf. Ser. **608**, 012045 (2015).
[121] M. Boronat, J. Fuster, I. Garcia, P. Roloff, R. Simoniello, and M. Vos, Eur. Phys. J. C **78**, 144 (2018).
[122] D. Arominski *et al.* (CLICdp Collaboration), arXiv:1812.07337.
[123] S. Catani, Y. L. Dokshitzer, M. H. Seymour, and B. R. Webber, Nucl. Phys. **B406**, 187 (1993).
[124] T. Ohl, Comput. Phys. Commun. **101**, 269 (1997).
[125] E. Leogrande, P. Roloff, U. Schnoor, and M. Weber, arXiv:1909.12728.
[126] P. S. Bhupal Dev and A. Pilaftsis, J. Phys. Conf. Ser. **873**, 012008 (2017).
[127] T. Plehn and M. Spannowsky, J. Phys. G **39**, 083001 (2012).
[128] T. Plehn, G. P. Salam, and M. Spannowsky, Phys. Rev. Lett. **104**, 111801 (2010).
[129] F. Kling, T. Plehn, and M. Takeuchi, Phys. Rev. D **86**, 094029 (2012).
[130] G. Kasieczka, T. Plehn, T. Schell, T. Strebler, and G. P. Salam, J. High Energy Phys. 06 (2015) 203.
[131] L. G. Almeida, S. J. Lee, G. Perez, I. Sung, and J. Virzi, Phys. Rev. D **79**, 074012 (2009).
[132] G. D. Kribs, A. Martin, T. S. Roy, and M. Spannowsky, Phys. Rev. D **81**, 111501 (2010).
[133] G. D. Kribs, A. Martin, T. S. Roy, and M. Spannowsky, Phys. Rev. D **81**, 111501 (2010).
[134] S. Yang and Q.-S. Yan, J. High Energy Phys. 02 (2012) 074.
[135] T. Plehn, M. Spannowsky, M. Takeuchi, and D. Zerwas, J. High Energy Phys. 10 (2010) 078.
[136] T. Plehn, M. Spannowsky, and M. Takeuchi, Phys. Rev. D **85**, 034029 (2012).
[137] D. E. Kaplan, K. Rehermann, M. D. Schwartz, and B. Tweedie, Phys. Rev. Lett. **101**, 142001 (2008).
[138] CMS Collaboration, Report No. CMS-PAS-JME-09-001, 2009.
[139] N. Alipour Tehrani and P. Roloff, Report No. CLICdp-Note-2014-002, 2014.
[140] R. Barate *et al.* (ALEPH Collaboration), Phys. Lett. B **495**, 1 (2000).
[141] A. Muennich, Report No. LCD-Note-2010-009, 2010.